Journal of Materials Chemistry A

Charge Transfer States and Carrier Generation in 1D Organolead Iodide Semiconductors

Journal:	*Journal of Materials Chemistry A*
Manuscript ID	TA-ART-04-2021-003325.R1
Article Type:	Paper
Date Submitted by the Author:	08-Jun-2021

Complete List of Authors:	Amerling, Eric; University of Utah, Chemistry Zhai, Yaxin; National Renewable Energy Laboratory Larson, Bryon; National Renewable Energy Laboratory Yao, Yi; Duke University Fluegel, Brian; National Renewable Energy Laboratory Owczarczyk, Zbyslaw; National Renewable Energy Laboratory, National Center for Photovoltaics Lu, Haipeng; National Renewable Energy Laboratory Whittaker-Brooks, Luisa; University of Utah, Chemistry Blum, Volker; Duke University, Blackburn, Jeffrey; NREL,

Charge Transfer States and Carrier Generation in 1D Organolead Iodide Semiconductors

Eric Amerling,[1,2] Yaxin Zhai,[1] Bryon W. Larson,[1] Yi Yao, [3] Brian Fluegel, [1] Zbyslaw Owczarczyk, [1] Haipeng Lu, [1] Luisa Whittaker-Brooks, [2] Volker Blum, [3] Jeffrey L. Blackburn[1,]*

1. *National Renewable Energy Laboratory, Golden, CO 80401*
2. *University of Utah, Salt Lake City, UT 84112*
3. *Thomas Lord Department of Mechanical Engineering and Materials Science, Duke University, Durham, NC 27708*
4. *University of North Carolina at Chapel Hill, Chapel Hill, NC 27599*

ABSTRACT

Excited-state interactions between organic and inorganic components in hybrid metal halide semiconductors open up the possibility of moving charge and energy in deliberate ways, including energy funneling, triplet energy harvesting, or long-lived charge separation. In this work, we utilize π-conjugated naphthalene diimide electron accepting molecules to fabricate a hybrid one-dimensional (1D) lead iodide semiconductor ((NDIC2)Pb_2I_6) with an internal charge separating junction. Despite recent efforts on the synthesis of 1D metal halide semiconductors, little is known about their electronic structure, optical properties, and excited-state dynamics. Steady-state and time-resolved spectroscopy measurements of ((NDIC2)Pb_2I_6) thin films elucidate discrete optical features from the lead iodide and naphthalene diimide components of this heterostructure, along with a weakly bound optically active charge transfer state. The type-II heterojunction between the organic NDIC2 and inorganic Pb_2I_6 moieties facilitates rapid separation of photogenerated charges, where charge recombination is hindered by the spatial separation of charges across the organic/inorganic interface. Our study also provides some important insights into the ways in which Coulomb interactions between the organic and metal halide moieties and π–π interactions between the organic cations can affect the crystallization of these hybrid semiconductors with large, optically active π-conjugated chromophores. We believe our findings will further enable the rational design of low-dimensional organic-inorganic heterostructures where the dielectric environment, charge transfer states, and exciton behavior may be modulated.

Introduction

The rational design and controlled assembly of molecular organic-inorganic heterostructures have been studied intensively within the materials science community. In these heterostructures, exotic physical and chemical functionalities may emerge due to the nontrivial combination of organic and inorganic components *via* covalent, ionic, or non-covalent interactions (e.g., van der Waals (vdW) forces and hydrogen bonding). From the family of organic-inorganic molecular compounds, organometal halides have received tremendous attention due to their tantalizing potential of revolutionizing the photovoltaic industry. For example, three-dimensional (3D) organolead halides have been incorporated into solar cells and have achieved efficiencies as high as 25.2%.[1] Strong quantum confinement in 2D organolead halide quantum wells, 1D quantum wires or 0D quantum dots leads to bound electron-hole pairs (excitons)[2, 3] as the fundamental excited state generated by photon absorption. These low-dimensional hybrid semiconductors are being explored for a wide variety of optoelectronic[4, 5] and spintronic devices.[6-9]

Regardless of the dimensionality, the organic cations in low-dimensional metal halide semiconductors (MHS) are often based on optically and electronically inert aliphatic ammonium moieties that primarily serve to insulate the metal halide structures from each other. The pioneering studies of Mitzi *et al.*[10] and Era *et al.*[11] demonstrated that replacing aliphatic organic cations with π-conjugated organic cations yields MHS with tunable bandgaps and facile charge/energy transfer across organic/inorganic interfaces. These seminal works showed that the organic species can in fact participate in the optoelectronic character of MHS when conjugation is present and and since then have inspired many research efforts on the fabrication of heterostructures that incorporate optically and electronically active π-conjugated organics.[10-21] If the frontier orbitals of π-conjugated organics are chosen appropriately, they can establish a type-II band alignment at the organic/inorganic interface, where a thermodynamic driving force exists for transfer of one type of charge carrier (electron or hole) into the organic cation and transfer of the other carrier into the metal halide.[10, 18-21] When such charge transfer (CT) interactions occur, they can assist in overcoming the strong exciton binding energy in these materials, especially in lower dimensional MHS, where this barrier to producing long-lived and useful free charges after excitation trends inversely with dimensionality (i.e. Coulomb binding for 3D < 2D < 1D < 0D).

A number of 1D MHS with tunable optoelectronic functionality have been synthesized in recent years,[22] including materials featuring a type-II band structure at the organic/inorganic interface. The type-II 1D structures primarily utilize viologen-based π-conjugated organic cations (e.g. methylviologen (MV^{2+})), since they are strong electron acceptors with deep lowest unoccupied molecular orbital (LUMO) levels.[13, 14, 19, 20, 23] Interestingly, several of these compounds feature low-energy optical transitions that have been assigned to CT excitations involving the conduction band of the inorganic framework and the LUMO of the organic molecules.[23] Furthermore, photoconductance and electron paramagnetic resonance (EPR) measurements demonstrate that optical excitation of these hybrid semiconductors can generate long-lived charge-separated states.[20] These intriguing measurements provide initial insight into the impact on optoelectronic performance, but more questions remain about whether different π-conjugated organic cations having different inter- and intramolecular motifs present can support these early observations as being more general. Additionally, despite a number of structural and steady-state spectroscopy studies, detailed time-resolved studies of MHS CT hybrids are exceedingly rare, leaving many open questions as to the spectroscopic signatures and transient dynamics of CT states and the degree to which charges remain Coulombically bound across the organic/inorganic interface following charge transfer. Rigorously characterizing, assigning, and ultimately understanding the complex organic/inorganic excited-state energy landscape in low dimensional MHS should enable researchers to more strategically navigate the vast choice of cation space, accelerating technology development based on this fascinating material class.

In this study, we demonstrate that 1,4,5,8-naphthalene diimide (NDI)[3, 24-28] based diammonium cations can be utilized to produce 1D organic/inorganic MHS with internal charge separation *via* CT states that lie energetically below the metal-halide excitonic absorption. Although the structural properties of 1D NDI-based MHS have been previously investigated,[28] there have been no efforts to elucidate the electronic structure or the dynamics of photoexcited excitons and/or charge carriers in these hybrid semiconductors. We find that an organized 1D structure forms within spin-coated thin films when naphthalene diimide diethylammonium (NDIC2) cations are templated around Pb_2I_6 wires at elevated annealing temperatures. This orients the π-conjugated NDI core in a way that facilitates the formation of optically active transitions energetically below the 1D lead iodide exciton transition. Pump wavelength-dependent transient absorption (TA) spectroscopy reveals an optical transition ca. 270 meV below the 1D lead iodide

exciton that is consistent with a CT state involving orbitals on the organic and inorganic frameworks. Hybrid density-functional theory (DFT) calculations also indicate the existence of such a CT state. Temperature-dependent PL spectroscopy suggests that this CT exciton can emit radiatively at low temperature (5K), but is dissociated above ca. 100 K due to a small binding energy. Consistently, time-resolved microwave conductivity (TRMC) suggests that some fraction of photogenerated excitons are dissociated into free carriers at room temperature. The experimental results are all consistent with the presence of a thermodynamic driving force for photoinduced charge separation, whereby electrons are transferred to the NDI LUMO and holes remain on the lead iodide framework. These results, and our rigorous assignments of spectral signatures, provide significant groundwork in developing design rules and systematic structure-function correlations for CT state energies and dynamics for self-assembled 1D MHS that incorporate π-conjugated organics.[29, 30]

Results

The organic cation used in this study is naphthalene diimide diethylammonium (NDIC2; **Figure 1A**). In contrast to common alkyl chain organic cations used in conventional organic inorganic metal halide semiconductors, NDIC2 is large, rigid, and has a significant π-bonding system that strongly influences the resulting orientation of the molecules.[31-33] The attractive aggregation forces of the NDI cations do not allow the formation of the typical 2D structure with corner-sharing lead iodide octahedra.[3, 34] Instead, NDI organic/inorganic hybrids assemble in a 1D metal halide polymorph featuring a combination of corner-, edge-, and face-sharing modes within the lead iodide chains. We grew single-crystals of naphthalene-based lead iodide wires through a common antisolvent technique.[35-39] The wires appear brown to black, presumably due to absorption across the visible range of the spectrum, as is observed for thin films (*vide infra*). The single-crystal structure of $[(NDIC2)_2Pb_5I_{14}(DMF)_2]\cdot 4DMF$ is shown in **Figure 1B**; this view normal to the *bc* plane is meant to highlight the orientation of the NDIC2 cations. Crystallographic data and structure refinement information are shown in Table S1.The Pb_2I_6 chains are decorated with NDIC2 cations, stacked in an H-aggregate-type structure where the naphthalene diimide cores align face-on to each other with separation of 3.7 Å, consistent with the vdW gap of π-stacked organic chromophores. DMF molecules are H-bonded to the ammonium groups on the NDIC2

cations in the single-crystal. Any attempts to remove the DMF, either by solvent soaks or vacuum drying, results in samples unsuitable for single-crystal diffraction analysis.[28]

Uniform 1D hybrid wire thin films of (NDIC2)Pb_2I_6 were spin-coated onto glass substrates from a DMF precursor solution. In **Figure 1C**, the (NDIC2)Pb_2I_6 thin film x-ray diffraction spectrum (red line, top) is compared to the simulated powder diffraction pattern (black line, bottom), derived from single-crystal diffraction. In the thin film sample, we see two strong peaks at 2θ = 7.5° and 7.9° that correspond to reflections associated with the (010) and (100) crystallographic planes, respectively, of the single-crystal structure. We believe that while DMF molecules may have some influence on the orientation of the NDIC2 cations, they do not inhibit the formation and spacing of the Pb_2I_6 chains (*vide infra*).

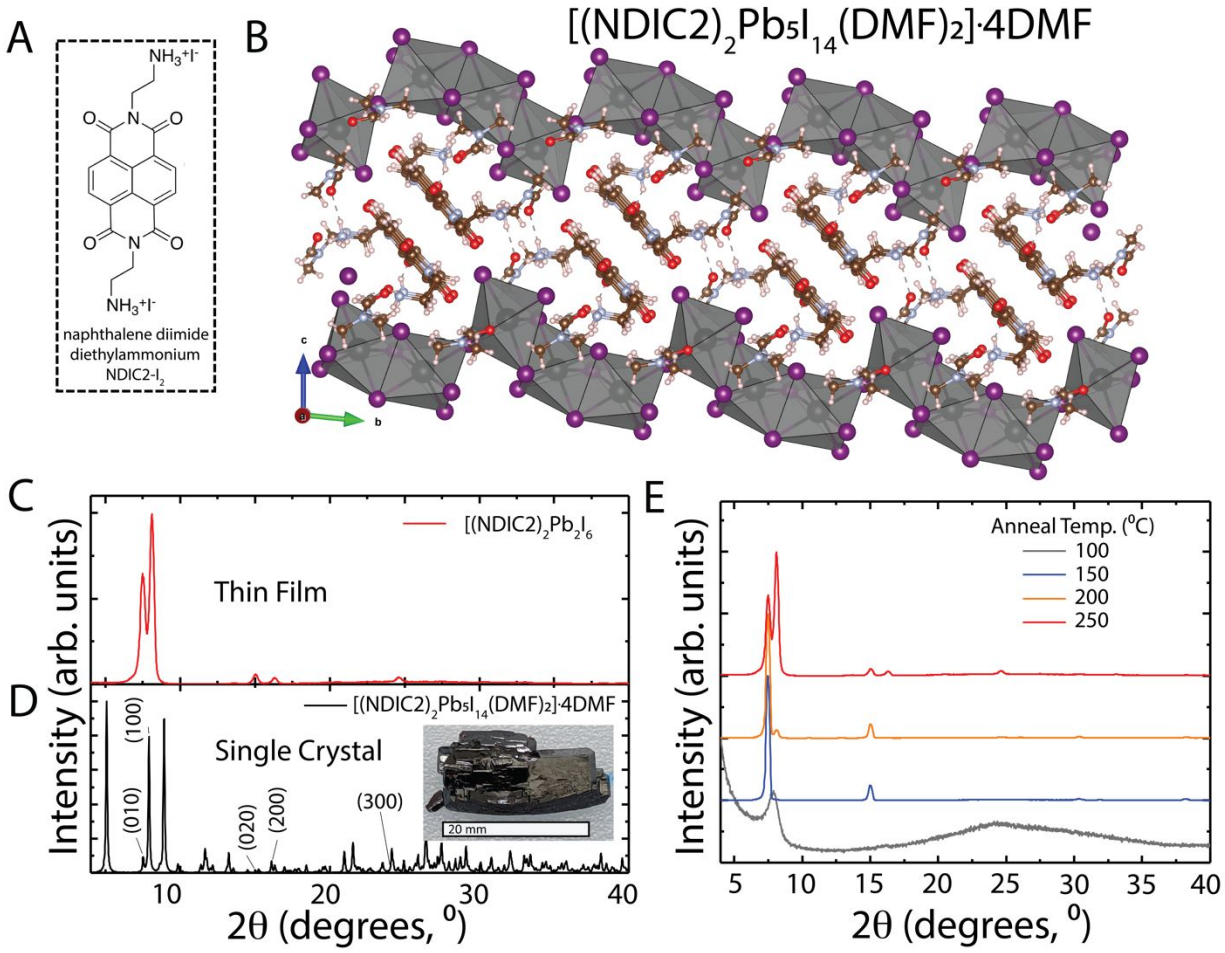

Figure 1. (A) Chemical structure for naphthalene diimide diethylammonium iodide (NDIC2-I_2). (B) Crystal structure of (NDIC2)Pb_2I_6 solvated with DMF. This view highlights the NDIC2 dications face-on stacking within the structure. Inset shows atomic distances between NDIC2 molecules (3.7 Å) and NDIC2 and Pb_2I_6 octahedra (3.9 Å). (C) Thin film X-ray diffraction spectrum of (NDIC2)Pb_2I_6 (red line) and (D) the simulated [(NDIC2)$_2$$Pb_5I_{14}(DMF)_2$]·4DMF (black line) powder X-ray diffraction spectrum. Inset shows a photograph of a dark brown as grown crystal. (E) Thin film X-ray diffraction spectrum of (NDIC2)Pb_2I_6 as a function of annealing temperature.

Since previous thermogravimetric (TGA) studies by Tremblay *et al.* revealed that DMF is released from the single-crystal $[(NDIC2)_2Pb_5I_{14}(DMF)_2]\cdot 4DMF$ at around 240 °C, we annealed our thin films at temperatures ranging from 100 to 250 °C.[28] We hypothesize that due to the large and sterically hindered nature of the NDIC2 di-cation, a higher rearrangement energy (input in the form of annealing temperature) may be required to orient the NDIC2 cations around the Pb_2I_6 wires in order to form a crystalline structure within the rapidly spin-coated thin film. The XRD pattern of 1D $(NDIC2)Pb_2I_6$ thin films is plotted in **Figure 1E** as a function of annealing temperature. The XRD pattern after annealing at 100 °C exhibits one broad peak centered around 7.8° followed by a much larger background scattering feature, which is indicative of the disordered nature of the film. Upon annealing at 150 °C, the structure within the thin film becomes more crystalline as evidenced by the appearance of two diffraction peaks at 7.5° and 15°, which correspond to reflections associated with the (010) and (020) crystallographic planes. The presented diffraction pattern resembles other 1D Pb_2X_6 hybrid quantum wire materials with similar lattice d-spacing, giving us confidence that the proposed lattice planes are assigned correctly.[40, 41] Further annealing at 200 °C induces the evolution of an additional diffraction peak at 7.9° which corresponds to the (110) crystallographic plane. Interestingly, the intensity of the diffraction peak of the (110) crystallographic plane increases when the thin films are annealed at 250 °C. We believe that at this temperature, the $(NDIC2)^{2+}$ dications have enough energy to fully crystallize and anisotropically order, using the Pb_2I_6 wires as a template. The films uphold the expected 1:3 ratio of I to Pb of the $(NDIC2)Pb_2I_6$ structure throughout annealing up to 250 °C, confirmed by SEM-EDX investigations (**Figure S1**). Additionally, since previous TGA analysis showed that NDIC2 decomposes around 400–500 °C, the observed structural changes should not reflect any sort of thin-film decomposition.[28]

Similar to the XRD pattern, the absorption of $(NDIC2)Pb_2I_6$ thin films also evolved as a function of annealing temperature (**Figure 2A,B**). At all annealing temperatures, the spectrum is dominated by a sharp resonance with a peak position (395 – 409 nm, or 3.03 – 3.14 eV) that is consistent with other similar 1D hybrid organic-inorganic materials[13, 23, 42] and is assigned to 1D excitons confined to the $[Pb_2I_6]^{2-}$ inorganic chains. Several changes occur as the annealing temperature is increased. Here, the exciton resonance redshifts by around 110 meV and we see the appearance of broad absorption below the exciton resonance in energy. These changes coincide with the evolution towards better long-range ordering, as deduced from the temperature-dependent

XRD (**Figure 1E**) and large changes to a neat NDIC2-I_2 film over the same temperature range. As such, we interpret the changes as arising from the impacts of NDIC2 cation and Pb_2I_6 wire orientation/ordering at elevated temperatures. We hypothesize that the exciton resonance's redshift arises from the NDIC2 cations orienting around the Pb_2I_6 wires and better isolating them within the low-dielectric organic sublattice. This structural rearrangement would thus enhance the dielectric confinement felt on the exciton, increasing its exciton binding energy.

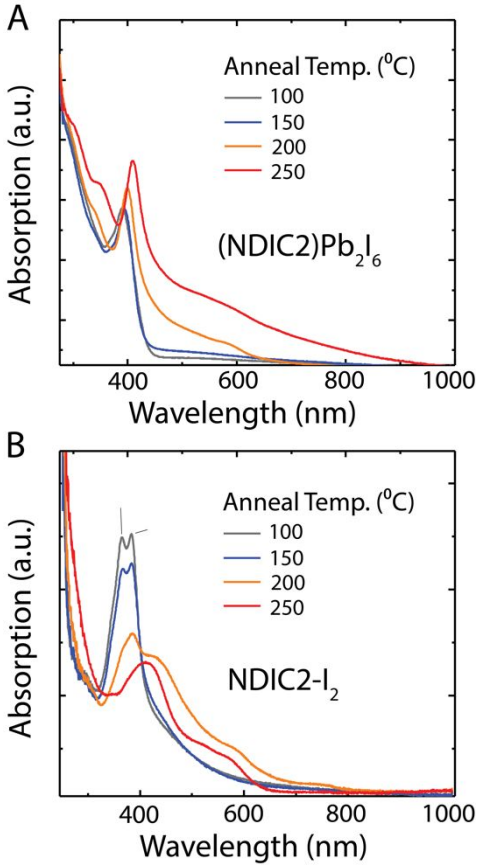

Figure 2. Thin film absorption as a function of annealing temperature of (A) (NDIC2)Pb_2I_6 and (B) NDIC2-I_2.

Low-dimensional metal halides typically have a sharp excitonic resonance as the lowest energy absorption.[43, 44] However, in (NDIC2)Pb_2I_6, we observe substantial absorption below the exciton transition energy that grows in with increasing annealing temperature. This increased sub-exciton absorption has two potential sources that we investigate in more detail below by transient absorption. First, this peak shares some similarities with the absorption peak observed for an annealed NDIC2-I_2 film, (**Figure 2B**), where the broad full-width at half-maximum (FWHM) and bathochromic shift (relative to neat NDIC2-I_2 in solution) are associated with strong, attractive π-π inter-molecular interactions for NDI H-aggregates.[45] Such broad absorption features are not

observed for NDIC2 in DMF solution (**Figure S2**). Thus, we conclude that interactions between electronically coupled NDIC2 molecules may contribute to the low-energy absorption in the (NDIC2)Pb_2I_6 samples. This possibility is consistent with the single-crystal data **(Figure 1B, inset)** that show H-aggregate-like stacking between adjacent $(NDIC2)^{2+}$ cations, with a plane-to-plane core distance of 3.7 Å between NDIC2 molecules. Second, this broad low-energy peak is also similar to the broad red-shifted absorption observed for 1D viologen-templated lead-iodide based CT heterojunctions.[23, 46] In this case, the low-energy transition is proposed to occur from the valence band of the lead iodide chain to the LUMO of the organic molecule.

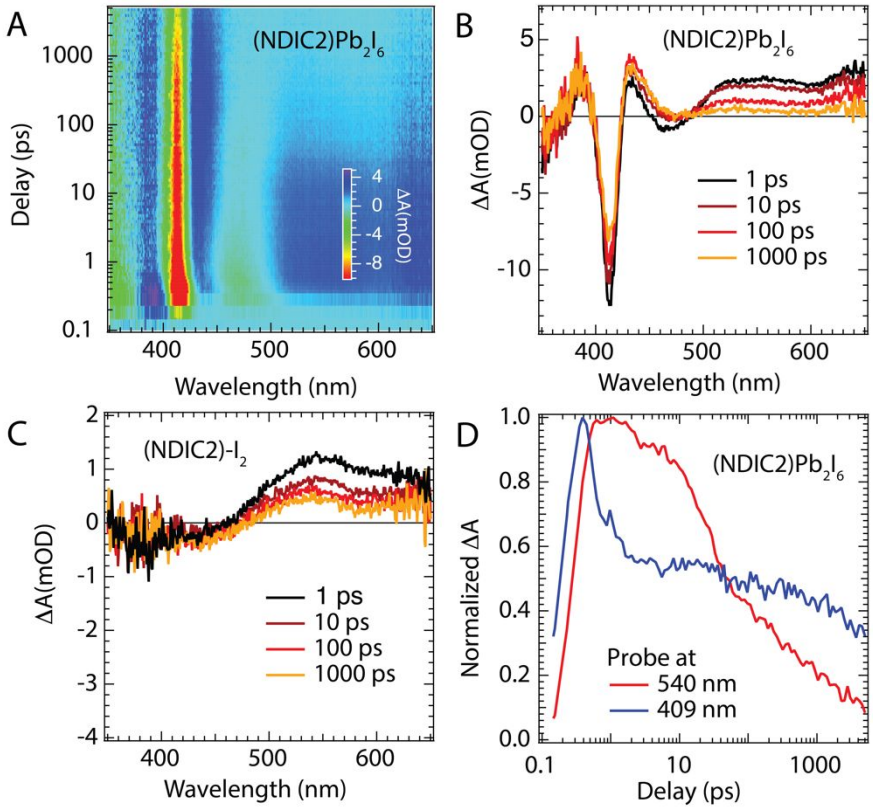

Figure 3. (A) Pseudo-color image of the transient absorption (TA) spectra for (NDI)Pb_2I_6 thin film. The horizontal and vertical axes are the probe-photon wavelength and pump–probe delay, respectively. The color intensity indicated by the scale bar represents the TA signal magnitude. (B-C) The TA spectra at different time delay for (B) (NDI)Pb_2I_6 and (C) NDIC2-I_2 films. (D) Decay dynamics of (NDIC2)Pb_2I_6 thin film probed at photo-induced absorption (PIA) peak at 540nm and photo-bleach peak (PB) at 409 nm.

To better understand the states available to, and the dynamics of, photogenerated excitons and charges in (NDIC2)Pb_2I_6, we performed ultrafast transient absorption (TA) spectroscopy. **Figure 3A** shows a pseudo-color 2D map of the temporal evolution of the TA spectra for the (NDIC2)Pb_2I_6 thin film, following excitation with a 380 nm pump pulse. **Figures 3B** and **3C**, respectively, show TA spectra of (NDIC2)Pb_2I_6 and NDIC2-I_2 films at delay times of 1, 10, 100, and 1000 ps. There

are three prominent features in the (NDIC2)Pb_2I_6 spectrum – a sharp exciton photobleach at 409 nm, a broad photobleach centered at 460 nm, and photoinduced absorption (PIA) feature centered around 550 nm. The only TA feature that is shared by both (NDIC2)Pb_2I_6 (**Figure 3B**) and NDIC2-I_2 (**Figure 3C**) is the PIA rising around 550 nm. Thus, this feature is linked to the NDI molecules themselves rather than any states associated with the Pb_2I_6, and has been attributed in several studies to the photoexcited NDIC2$^{\bullet-}$ radical anion.[3, 29, 47, 48] Although the precise mechanism the NDIC2$^{\bullet-}$ radical anion formation has not been elucidated, studies have suggested that there is a photoinduced electron transfer from the iodide to the NDIC2 cation.[3, 49] Interestingly, the observation of the NDIC2$^{\bullet-}$ radical anion suggests that 380 nm excitation of the (NDIC2)Pb_2I_6 ultimately results in some population of electrons on the organic molecules.

The dynamics of the 1D Pb_2I_6 photobleach (probed at 409 nm) and NDIC2 cation PIA (probed with 540 nm), after pumping at 380 nm, are shown in **Figure 3D**. The 1D exciton photobleach (blue line **Figure 3D**) rises rapidly on the time scale of the instrument response (ca. 200 fs), consistent with sub-picosecond exciton generation commonly observed for metal halides.[3] Rapid decay of the exciton photobleach over the first picosecond coincides with a similar ca. 1 ps rise time of the PIA at 540 nm, assigned to the NDIC2$^{\bullet-}$ radical anion. This coincidence suggests that the initially excited 1D excitons on the Pb_2I_6 rapidly evolve, on the picosecond time scale, into a charge-separated state ([NDIC2$^{\bullet-}$][$Pb_2I_6^+$]) that consists of an electron on the NDIC2 molecule(s) and a hole that remains on the Pb_2I_6 wire. Beyond 1 ps, the 1D exciton bleach decays very slowly, with ca. 35% of the initially generated photobleach still remaining after 4 ns. This bleach decay is much slower than what is typically observed for e.g. 2D Ruddelsden-Popper or Dion-Jacobson hybrid perovskites (we could not find TA studies on 1D lead-iodide hybrids to compare to), which typically show nearly complete recovery of the ground state within similar time scales. It is important to note here that either excitons or charge carriers (or both) can bleach the 1D exciton transition.[50-52] As such, we attribute the photobleach observed beyond 1 ps to holes remaining on the Pb_2I_6 wire, where the slow ground state recovery is consistent with spatial separation of the photoexcited electron and hole and the associated hindrance to recombination of the separated charge carriers. Consistently, the PIA at 540 nm is also long-lived, reflecting the lifetime of electrons localized onto the conjugated core of NDIC2 following CT.

To understand the origin of the photobleach centered at 460 nm, we varied the pump wavelength in TA experiments. We chose pump wavelengths on the red edge of this transition,

ranging from 480 nm to 540 nm, to ensure that we were sufficiently low in energy so as not to directly excite the 1D exciton transition centered at 409 nm. A strong photobleach from the 1D exciton appears instantaneously when pumped between 480 and 520 nm (**Figure 4A**); 2D TA maps for each pump wavelength are shown in **Figure S3**. This observation suggests that the optical transitions centered at 409 nm and 460 nm share the same ground state. As such, we propose that this 460 nm optical transition corresponds to the generation of a CT exciton, where the exciton is composed of one charge carrier that resides on the lead-iodide framework and one carrier that resides on the NDIC2 molecule. Based on our proposed mechanism of CT discussed above, we suggest that this CT exciton would consist of an electron localized on the NDIC2 molecule(s) and a hole localized on the Pb_2I_6 wire. Consistently, previous density functional theory (DFT) calculations of similar Pb_2I_6 1D hybrid materials, such as $MVPb_2I_6$ (MV^{2+}: N,N'-dimethyl-4,4'-bipyridinium, also known as methylviologen)[19] and $(Pb_2I_6)\cdot(H_2DPNDI)\cdot(H_2O)\cdot(NMP)$ (DPNDI: N,N'-di(4-pyridyl)- 1,4,5,8-napthalene diimide; NMP: N-methylpyrrolidin-2-one),[53] found that the VB of these materials is dominated by lead *s* orbitals and iodine *p* orbitals whereas the CB is dominated by the oxygen and nitrogen *p* orbitals of the organic cation. If we adopt this picture for our assignment, the concept of phase-space filling dictates that excitation of the low-energy CT exciton should contribute to a bleach of the 1D exciton transition since the same lead and iodine VB orbitals contribute to both of these optical transitions.

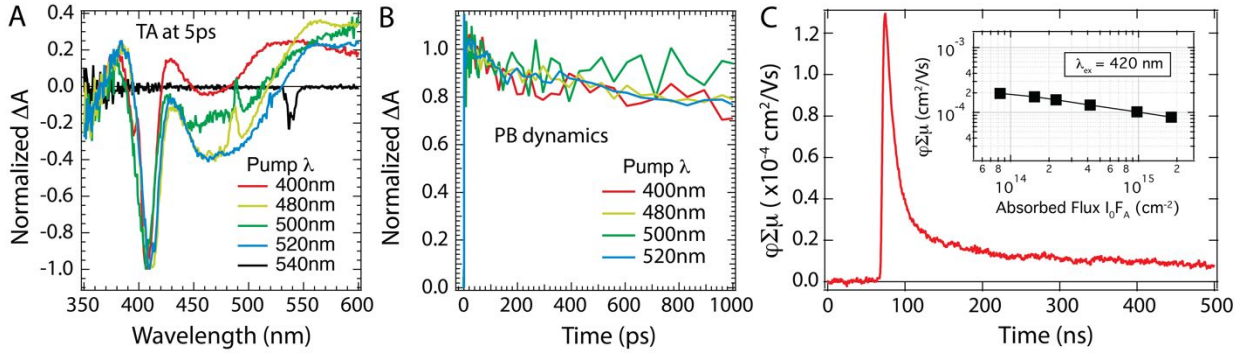

Figure 4. Transient absorption (TA) of $(NDI)Pb_2I_6$ thin film pumped at various wavelength. **(A)** TA spectra at 5 ps. Normalized at 405nm. **(B)** Dynamics of the 409 nm exciton bleach, following excitation at different wavelengths. Transients are normalized at 1ps. **(C)** TRMC transient decay at absorbed photon flux of 4.2×10^{14} (420 nm). Inset: excitation fluence-dependent peak yield mobility product excited at 420 nm.

The 409 nm exciton photobleach is no longer observed when pumped at 540 nm (**Figure 4A**, black trace), suggesting that the red edge of the CT state is around 520 nm and that steady-state absorption features beyond ca. 520 nm are not electronically coupled to the Pb_2I_6 framework. Based on these results and the width of the broad low-energy photobleach observed in

(NDIC2)Pb_2I_6 TA spectra, we conclude that a broad CT absorption spans from ca. 430 nm to 520 nm. In contrast, NDIC2 molecules that are electronically coupled with each other, but are poorly coupled to the Pb_2I_6 framework, lead to states absorbing beyond 520 nm. **Figure 4B** demonstrates that an identical slow ground-state recovery, measured by the dynamics of the 409 nm bleach, is observed when pumping the 1D exciton or the low-energy CT state, consistent with each state ultimately producing the same charge-separated state. Interestingly, the NDIC2$^{\bullet-}$ dynamics at 540 nm are distinct from the dynamics of the 1D exciton up to ca. 1 ns (**Fig. 3D**), suggesting that there is some evolution of the nature of charges on the NDIC2 molecules over this time frame. After ca. 1 ns, the dynamics of the two states are similar, and most likely reflect the kinetics of electron-hole recombination across the organic/inorganic interface.

The apparent generation of a charge-separated state in TA measurements led us to search for photoconductance in the (NDIC2)Pb_2I_6 hybrid. Charges can remain Coulombically bound across the organic-inorganic interface as a localized charge transfer exciton or can escape the Coulomb attraction to produce separated charges with some degree of mobility. TA measurements cannot typically distinguish between these two possibilities. To probe this question, we performed flash-photolysis time-resolved microwave conductivity (fp-TRMC) to probe free carrier generation and dynamics. TRMC is a contactless, optical pump-continuous microwave probe measurement that is sensitive to the presence of free mobile charges. Thus, excitons, and other Coulomb-bound carriers are not detected with this technique.[54, 55] Due to the contactless nature of this technique, TRMC yield-mobility products can probe local free carrier generation, even in semiconductors where long-range transport is difficult or impossible to measure with contact-based techniques. Therefore, TRMC provides fundamental information about the maximum potential free carrier generation and mobility that can be expected in a novel material.[56]

By measuring the photoinduced change in microwave conductance (ΔG_{photo}) of the sample, we can obtain the yield-mobility product ($\phi\Sigma\mu$) of photoinduced carriers, based on the equation:

$$\Delta G_{photo} = \beta e I_0 F_A \phi \sum \mu$$

where β is related to the dimensions of the waveguide cross-section, e is the elementary charge, I_0 is the flux of the incident photon, and F_A is the fraction of light absorbed by the sample, and ΔG_{photo} is end-of-pulse peak photoconductance value.[57, 58] The TRMC photoconductance transient at an absorbed photon flux of 4.2×10^{14} (420 nm) is shown in **Figure 4C** and the excitation

fluence-dependent yield mobility product is shown in the inset. We used a 420 nm pulse to excite as close the Pb_2I_6 exciton as our experimental setup would allow. The results show that there is free carrier generation when exciting into the exciton (420 nm), which is unexpected in this confined 1D system. The free carrier generation implies that the photoinduced CT event deduced from TA measurements does not result solely in a Coulomb-bound CT exciton. The excitation produces long-lived photoconductance signals that decay over long time scales (i.e. beyond 100 ns), consistent with the conclusion that the recombination of carriers is slowed by the spatial separation of the electron on NDI molecules and the hole on the Pb_2I_6 wire.

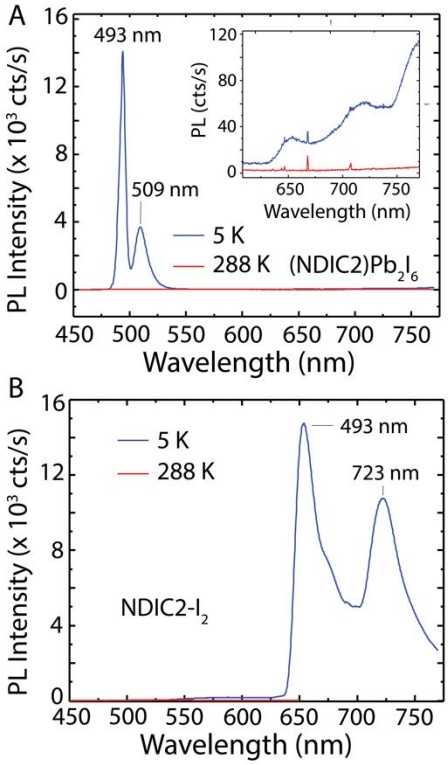

Figure 5. (A) Emission spectrum from (NDIC2)Pb_2I_6 thin films at 288K (red line) and 5K (blue line) Expanded view at long wavelengths in inset. (B) Neat NDIC2-I_2 thin film emission spectrum at 288K (red line) and 5K (blue line).

Our TA and TRMC results demonstrate that photoexcitation of the hybrid ultimately produces separated charges that recombine on a relatively long time scale. This suggests that the binding energy of the proposed CT exciton, accessible via direct absorption at ca. 460 nm, is sufficiently low that it does not remain bound at room temperature. To explore the binding energy of this CT exciton in more detail, we turn to temperature-dependent PL spectroscopy. At room temperature, no PL is observed in the (NDIC2)Pb_2I_6 thin film (**Fig. 5A**, red trace). Based on our time-resolved spectroscopy results discussed above, we propose that the PL is quenched by charge separation

between the NDIC2 and the Pb_2I_6 chains. PL emission suppression due to charge separation has been observed in other naphthalene diimide/lead halide hybrid structures[3, 24, 25, 27] as well as 2D $CsPbBr_3$ nanoplatelets decorated with perylene diimide ligands.[34]

Notably, we observe narrow emission from the (NDIC2)Pb_2I_6 thin films at 5K (**Fig. 5A**, blue trace), where two peaks at 493 nm and 509 nm are discerned. These peaks (1) have huge Stokes shifts (ca. 500 – 600 meV) relative to the 409 nm exciton absorption, and (2) do not spectrally overlap with the low-temperature emission from an NDIC2 film (653 nm and 723 nm, **Figure 5B**). The peaks are, however, situated just on the low-energy side of the broad peak observed in TA measurements that we assign to the CT exciton. As such, we assign these peaks to emission from the CT state. We suggest a few potential mechanisms for the origin of *two* emissive peaks: (1) slight changes in molecular interactions of the NDIC2 molecule and the Pb_2I_6 wires within the (100) and (010) crystallographic planes may induce a distribution of CT states due to the varying strength of the orbital overlap; (2) the bathochromic shift of the lower energy peak (509 nm), ca. 80 meV relative to the peak at 493 nm, arises from polaronic stabilization;[59] and (3) distinct transitions may exist from both the lead-iode VB and non-bonding orbitals to the NDIC2 LUMO.[13]

The full suite of temperature-dependent PL spectra of the (NDIC2)Pb_2I_6 thin film is shown in **Figure S4**. As the temperature is increased from 5K to 40K, the emission signal at 509 nm is significantly quenched, while the emission signal at 493 nm remains unchanged until 80K (after which it disappears). These results suggest that while the CT exciton remains as a bound e-h pair that can radiatively recombine at low temperatures (< 80 K) the CT exciton is dissociated at room temperature, due to thermal energy, and does not emit. Since the data in **Figure S4** do not follow a straightforward Arrhenius dependence, we cannot extract a reliable CT exciton binding energy. However, the disappearance of all PL emission above 80 K allows us to provide a rough estimate, based simply on thermal energy at 80 K (10 meV).

With this information, we hypothesize that a likely charge transfer mechanism, following excitation of the 1D Pb_2I_6 exciton transition, is the following: (1) photoexcitation around 409 nm generates the 1D Pb_2I_6 exciton, which (2) moves into the CT state and finally, (3) is split into free carriers where (4) the electron resides the NDIC2, and the hole resides on the Pb_2I_6 chain.

Figure 6 provides a summary of the conclusions we reach from consideration of the full suite of steady-state and time-resolved spectroscopy measurements. Taken as a whole, the TA data suggest that photons incident on the 1D (NDIC2)Pb_2I_6 hybrid can generate a variety of different

initial states, depending on the range of photon energies (**Figure 6A**). Photons in the range of the 1D exciton resonance at 409 nm generate excitons on the Pb_2I_6 framework (**Figure 6A/B-1**), a low-energy CT state is accessible to photons spanning the range of ca. 430 – 520 nm (**Figure 6A/B-2**), and photons >540 nm directly excite transitions isolated on coupled NDIC2 molecules (**Figure 6.A/B-3)**. Dynamic data suggest that all initially generated states rapidly evolve downhill in energy, ultimately generating the same long-lived charge-separated state $[NDIC2^{\bullet-}][Pb_2I_6^{+}]$.

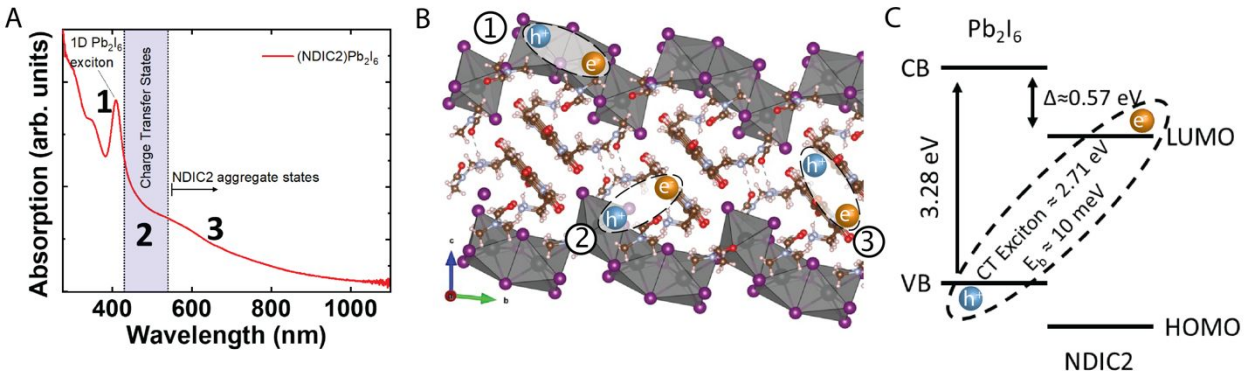

Figure 6. (A) Absorption spectrum of $(NDIC2)Pb_2I_6$ with 3 primary optical features labeled. (B) Schematic depicting the location of the (1) exciton, (2) CT states, and (3) NDIC2 aggregate states on the crystal lattice. **(C)** Proposed charge transfer energy diagram between Pb_2I_6 wires and NDIC2 cations.

The energy level diagram in **Figure 6C** outlines the proposed interfacial band alignment that facilitates charge transfer between the Pb_2I_6 wires and NDIC2 cations. From our absorption measurements, the 1D Pb_2I_6 exciton resonance is located at 409 nm (3.03 eV); if we estimate an exciton binding energy of around 250 meV for this exciton, based on other low dimensional metal halide exciton binding energies,[60-62] then the electronic gap (optical gap + exciton binding energy) can be placed around 3.28 eV. From our TA measurements, we observed the CT state centered at 460 nm (2.7 eV); therefore, we can assign this as the optical gap of the CT exciton. Lastly, the temperature-dependent PL measurements suggest that the exciton binding energy of this CT state is likely small (estimated at 10 meV). This places the electronic gap (2.7 eV optical gap + 10 meV exciton binding energy) of this CT exciton around 2.71 eV. Therefore, the difference in energy between the CB of Pb_2I_6 and LUMO of NDIC2 is approximately 570 meV. Since this energy difference exceeds the expected binding energy for the 1D Pb_2I_6, there is a thermodynamic driving force for electron transfer to adjacent NDI molecules, consistent with our observations.

Hybrid DFT calculations (FHI-aims all-electron code[63, 64], HSE06 density functional[65, 66], 25% short-range screened exchange, with spin-orbit coupling[67], see methods/SI for details) of the lowest energy electron and hole density distributions in the $[(NDIC2)_2Pb_5I_{14}(DMF)_2]\cdot 4DMF$

excited state (**Figure 7**) provide direct support of our hypothesis of the existence of a charge-separated state (FHI-aims all-electron code[63, 64], HSE06 density functional[65, 66], 25% short-range screened exchange and screening parameter 0.11 (Bohr radii)$^{-1}$, with spin-orbit coupling[67], see methods/SI for details). In this case, the hole is localized in the valence band minimum (VBM) of the lead iodide network, while the electron is localized on the (NDIC2) molecule. The HSE06 density functional with the above-mentioned parameters is known to provide a qualitatively correct description of the HOMO-LUMO gap of many inorganic semiconductors. However, it will underestimate the quasiparticle (transport) gap of large bandgap systems such as an organic moiety if interpreted based on self-consistent-field single particle eigenvalues only[68], as done in **Figure 7**, leading to a quantitatively too low energetic placement of the organic LUMO. A computed absorption spectrum is shown in **Figure S7**, showing residual weak absorption between the inorganic-derived VBM and the organic LUMO, despite its absolute location being underestimated. The underestimation of the charge-transfer gap can be qualitatively corrected by using a total-energy based approach to estimate the energy difference, with an actual electron on the molecular LUMO. Using a non-Aufbau occupation constrained DFT model[69-71], in which the electron and hole are localized in the same unit cell, we found that the charge-separated constrained state has an energy of 2.31 eV (536 nm). This value is closer to the red edge of our experimentally assigned CT state from transient absorption studies. It would be even more interesting to apply a many-body method accounting for the details of screening (such as the Bethe-Salpeter Equation or better), which is, however, not currently computationally feasible for the structure size of interest here. Even given the remaining uncertainties of constrained hybrid DFT methods for CT states, the overall theoretical result confidently confirms the formation of a charge transfer state.

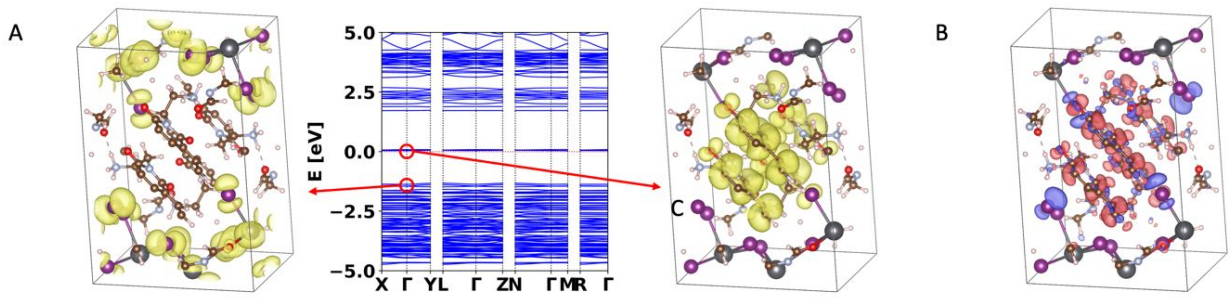

Figure 7. A. The HSE06+SOC band structure and the orbitals at VBM (left image) and CBM (right image) at the *Γ* point, for the $[(NDIC2)_2Pb_5I_{14}(DMF)_2]\cdot 4DMF$ crystal. The isosurface is shown for a 0.03 $1/Å^{3/2}$ norm of the orbitals. B. The electron density difference between the first excited state and the ground state by HSE06 calculation. The red/blue isosurface indicates a density difference of +/-0.075 electrons/$Å^3$. The first excited state was calculated by a non-Aufbau occupation, constraining both the CBM and the VBM to be half occupied.

Discussion

It is interesting to consider the degree to which the 1D (NDIC2)Pb_2I_6 structure is connected to the observation of optically active CT state(s) and long-lived charge separation across the organic/inorganic interface. It is important to note that a number of 2D Type-II metal halide semiconductors have been studied where no optically active CT states are observed below the exciton resonance, despite what appears to be rapid and efficient charge separation.[3, 10, 18] In contrast, our studies demonstrate that aromatic NDI molecules in a 1D lead-halide structure produce absorptive CT states similar to those observed for viologen-based 1D structures.[13, 14, 19, 20, 23] One key structural difference is that the 1D structure allows the molecules to orient roughly face-on with the lead-iodide wires, in contrast to the edge-on orientation that is typical for 2D structures. The face-on orientation in 1D structures is analogous to face-on transition-metal dichalcogenide/molecule heterojunctions that support charge separation and interfacial charge transfer states. For example, in copper phthalocyanine-MoS_2 heterojunctions, the π-face-on molecular orientation and further stacking of electronically coupled copper phthalocyanine molecules enables rapid hole migration away from the heterointerface, thereby decreasing the electron-hole Coulomb interaction. This led to a long-lived charge separated state of 70 ns, which is significantly longer than disoriented or edge-on-oriented molecules in a MoS_2 heterojunction.[72]

Charge separation in NDI based lead halide structures has also been observed in multilayer quasi-2D Ruddlesden Popper phases.[3] In the study by Proppe et al., films synthesized with a mixture of PbI_2, NDIC2, and methylammonium (MA) produced a mixture of weakly confined 2D perovskite and 1D structures. They observe a similar absorption onset to what we observe for (NDIC2)Pb_2I_6 thin films and acknowledge that this absorption onset could reflect the contribution of 1D phases. Based on our work here, it is possible that the low-energy absorption onset observed in that study may indeed contain contributions of the CT absorption within a (NDIC2)Pb_2I_6 1D phase. The impact of this 1D phase on their TA measurements is difficult to discern since the displayed spectral window does not include wavelengths below 480 nm. In general, our study suggests that future studies of mixed-phase MHS produced with large aromatic cations such as NDI should carefully consider the effects of optically active 1D CT states when assessing both phase purity and potential charge transfer mechanisms in time-resolved studies.

Based on these structural considerations, we speculate that enhanced orbital overlap between the aromatic π system of the organic and the orbitals of the lead iodide framework may

be a contributing factor to the observation of optically active CT states in 1D MHS with π-conjugated chromophores. Further, electronic coupling between the molecular chromophores, which is feasible in both 1D and 2D structures, is likely a key contributor to the stabilization and long lifetime of charge separation. Looking forward, it will be interesting to explore more hybrid 1D MHS with large aromatic chromophores since the geometric constraints on orbital mixing are relaxed relative to 2D. It will be interesting to systematically study the generality of such CT states as a function of molecular properties and ultimate MHS structure, as well as the degree to which CT state properties (transition energy, binding energy) are modulated by the relative geometries and associated orbital interactions at the organic/inorganic interface. Rigorously characterizing, assigning, and ultimately understanding the complex organic/inorganic excited-state energy landscape in low dimensional MHS should enable researchers to more strategically navigate the vast choice of cation space, accelerating technology development based on this fascinating material class.

Conclusions

In this work, we explore 1D metal halide semiconductors with large π-conjugated organic molecules with a plethora of structural and nonlinear optical characterizations. Temperature-dependent XRD and absorption studies demonstrate that the $(Pb_2I_6)^{2-}$ chains serve as templating 1D layers for the ordering and crystallization of the $(NDIC2)^{2+}$ organic moieties. Absorption, PL, and TAS studies on 1D (NDIC2)Pb_2I_6 demonstrate that: (1) an optically active CT state is formed, with absorption spanning from 480 to 520 nm, (2) the CT exciton has a low binding energy, (3) charge separation across the organic/inorganic interface occurs on the sub-picosecond time scale, and (4) the ground state is recovered on much longer time scales (> 5 ns). Hybrid DFT calculations provide additional evidence that such a charge-separated state is able to form. Finally, TRMC studies provide conclusive evidence of free charge carrier generation in this 1D (NDIC2)Pb_2I_6 molecular heterostructure. We hypothesize that the optically active CT state and long-lived charge separation may stem, at least in part, from the close proximity and face-on oriengation between the organic molecule and the inorganic lead iodide chains within the crystal structure. We believe that further functionalization of the NDI moiety may allow for the tailoring of optoelectronic properties of 1D NDI-based molecular heterostructures, potentially to fit desired applications in e.g. photovoltaics, sensing, etc. Given the strong evidence of free carrier generation in these systems, we encourage further studies pertaining to their device fabrication and characterization.

Acknowledgements

This work is primarily funded as part of the Center for Hybrid Organic Inorganic Semiconductors for Energy (CHOISE), an Energy Frontier Research Center funded by the Office of Science, Basic Energy Sciences within the US. DOE. E.A. gratefully acknowledges support from the Office of Science Graduate Student Research (SCGSR) fellowship. LW-B gratefully acknowledges support from the DOE Office of Science, Basic Energy Sciences under contract No. DESC0019041. This work was authored in part by the National Renewable Energy Laboratory (NREL), operated by Alliance for Sustainable Energy, LLC, for the U.S. Department of Energy (DOE) under Contract No. DE-AC36-08GO28308. This work used the Extreme Science and Engineering Discovery Environment (XSEDE), which is supported by National Science Foundation grant number ACI-1548562. This work used the Extreme Science and Engineering Discovery Environment (XSEDE) Bridges-2 at the Pittsburgh Supercomputing Center through allocation TG-DMR200077 and the Bridges-2 Early User Program.

Experimental / Computational

*Synthesis of 2,7-bis(2-ammoniumethyl)benzo[lmn][3,8]phenanthroline-1,3,6,8(2H,7H)-tetraone trifluoroacetate **(C)**.*

Naphthalenetetracarboxylic dianhydride (**A)** (5.36 g, 20 mmol), $H_2NCH_2CH_2NHBoc$ (7.06 g, 44 mmol), triethylamine (2.9 mL, 20 mmol) and dry NMP (75 mL) was stirred at 90 °C for 30 h. A warm mixture (45 °C) was slowly poured into 400 mL of ethyl acetate, precipitated solid was separated by filtration, washed 3 x 20 mL of ethyl acetate and dried under vacuum. Intermediate compound (**B).** 2,7-bis(2-ammoethyl)benzo[*lmn*][3,8]phenanthroline-1,3,6,8(2*H*,7*H*)-tetraone **(B)** as subsequently suspended in DCM (50 mL) before trifluoroacetic acid (15 mL) was added. The resulting mixture, which became briefly homogenous, was than stirred at gentle reflux for 6 h, DCM was removed, and the residue was mixed with of ethyl acetate (50 mL). Solid material was separated by filtration, washed 3 x 15 mL of ethyl acetate and dried under vacuum to yield 10.1 g (87%) of the title compound (**C).**

2,7-bis(2-ammoniumethyl)benzo[*lmn*][3,8]phenanthroline-1,3,6,8(2*H*,7*H*)-tetraone iodide (D).

Trifluoroacetate **C** (6.00 g, 10.3 mmol) was stirred at rt with 120 mL of 15% solution of KI in water for 1 h. Yellow solid material was separated by filtration, washed 2 x 15 mL of cold (1-3 °C) deionized water and dried at 50 °C under vacuum to yield the title compound in 81 % yield (5.07g). ^{1}H-NMR (400 MHz, DMSO-d6) δ = 8.72 (s, 4H, Ar-H), δ = 7.8H (bs, 6H, NH_3^+), δ = 4.35 (t, 4H, CH_2, J = 5.75 Hz), δ = 3.20 (t, 4H, CH_2, J = 5.75 Hz).

Thin film preparation

For UV-Vis absorption, photoluminescence, and transient absorption spectroscopy, traditional borosilicate glass substrates were used. For the TRMC measurements, quartz substrates were used. For SEM-EDX analysis, ITO coated glass was used. All substrates were cleaned successive sonication in detergent, DI water, acetone, and isopropyl alcohol, and finally subjected to oxygen plasma cleaning for 15 min. 0.19 M solutions of (NDIC2)Pb_2I_6 were prepared in by dissolving NDIC2-I_2 (45.6 mg) and PbI_2 (57.6 mg) in a 1:2 molar ratio in 1 mL of DMF. Solutions were heated at 60 ^oC for 30 min, or until completely dissolved. Thin films were spin coated at 1500 rpm for 30 sec and annealed at 250 ^oC, unless otherwise noted. All material fabrication was carried out in a nitrogen-filled glovebox.

Single-crystal growth

Details of antisolvent single-crystal growth of (NDIC2)Pb_2I_6 has been reported elsewhere.[28] Briefly, 75 mg of NDIC2-I_2 and 115 mg of PbI_2 were dissolved in 5 mL of dimethylformamide (DMF) by gently heating the solution at 60 ^oC for 30 min. The stir bar was then removed and the vial was then sealed inside of a larger jar with 10 mL of dichloromethane (DCM). The DCM displaced the DMF and caused the crystals to crash out. Crystallization occurred in about 12 hours, with suitable samples for single-crystal diffraction in about a week.

Characterization

X-ray diffraction (XRD) patterns (2θ scans) were obtained with Cu-Kα radiation. Absorption studies were performed on a Varian Cary 50 UV-Vis spectrophotometer. Room temperature and 5K photoluminescence (PL) measurements were performed using a 442 nm HeCd laser with an approximate power of 36 μW. SEM-EDX measurements were performed using 10kV accelerating voltage.

Single-Crystal Diffraction

Single-crystal diffraction data were collected on a Bruker D8 VENTURE at 100 K using gallium Kα X-rays (λ = 1.34 Å). A full sphere of diffraction data was collected and multi-scan empirical absorption correction was applied. Structure solution was obtained by direct methods using the SHELXS program and refined using the least-squares method by employing the SHELXL[74] program within the Olex2 software[75].

Time resolved microwave conductivity

Time-resolved microwave conductivity measurements were performed in a standard system that has been reported elsewhere.[57] Briefly, the sample on a quartz substrate was placed in a microwave cavity operating at ≈ 9 GHz. We photoexcite using a 5 ns laser pulse from an optical parametric oscillator pumped by the third harmonic of an Nd:YAG laser. The fractional change in the microwave power, P, in the cavity, due to absorption of the microwaves by the photoinduced free electrons and holes, is directly related to the photoconductance, ΔG, by $\Delta P/P = -K\Delta G$, where the calibration factor K was determined through numerical simulation of the cavity.

Transient Absorption Spectroscopy

The transient absorption measurement is based on the Ti:sapphire laser amplifier (Continuum Integra, 800 nm, pulse duration ~100 fs, ~3 mJ/pulse, and 1 kHz repetition rate) and the pump–probe transient reflection spectrometer (Helios, Ultrafast System). The fundamental laser pulse is generated by a Ti:sapphire amplifier and then split into two parts by a beam splitter. One beam is sent to an optical parametric amplifier to generate the pump pulse with tunable wavelength, and its intensity is attenuated by two neutral density filter wheels. The other part of the fundamental pulse is focused into a sapphire crystal to generate a white-light continuum (450–800 nm), which is used as the probe. The probe pulses are delayed in time with respect to the pump pulses using a motorized translation stage mounted with a retroreflecting mirror. The pump and probe are spatially overlapped on the surface of the sample. Both the pump and probe beam are normally incident on the sample. The size of the focused spot at the sample position for the probe and pump beams is around 200 and 600 μm, respectively.

Hybrid density functional theory calculations

Technical details are provided in the SI.

References

1. Nrel, Best Research-Cell Efficiency Chart | Photovoltaic Research | NREL. 2019.

2. Marchal, N.; Van Gompel, W.; Gelvez-Rueda, M. C.; Vandewal, K.; Van Hecke, K.; Boyen, H. G.; Conings, B.; Herckens, R.; Maheshwar, S.; Lutsen, L.; Quarti, C.; Grozema, F. C.; Vanderzande, D.; Beljonne, D., Lead-Halide Perovskites Meet Donor-Acceptor Charge-Transfer Complexes. *Chemistry of Materials* **2019,** *31* (17), 6880-6888.

3. Proppe, A. H.; Tremblay, M. H.; Zhang, Y. D.; Yang, Z. Y.; Quintero-Bermudez, R.; Kelley, S. O.; Barlow, S.; Marder, S. R.; Sargent, E. H., Naphthalenediimide Cations Inhibit 2D Perovskite Formation and Facilitate Subpicosecond Electron Transfer. *J Phys Chem C* **2020,** *124* (44), 24379-24390.

4. Amerling, E.; Baniya, S.; Lafalce, E.; Zhang, C.; Vardeny, Z. V.; Whittaker-Brooks, L., Electroabsorption Spectroscopy Studies of $(C_4H_9NH_3)_2PbI_4$ Organic-Inorganic Hybrid Perovskite Multiple Quantum Wells. *J Phys Chem Lett* **2017,** *8* (18), 4557-4564.
5. Amerling, E.; Baniya, S.; Lafalce, E.; Blair, S.; Vardeny, Z. V.; Whittaker-Brooks, L., Quantifying Exciton Heterogeneities in Mixed-Phase Organometal Halide Multiple Quantum Wells via Stark Spectroscopy Studies. *ACS Appl Mater Interfaces* **2020,** *12* (47), 52538-52548.
6. Long, G. K.; Jiang, C. Y.; Sabatini, R.; Yang, Z. Y.; Wei, M. Y.; Quan, L. N.; Liang, Q. M.; Rasmita, A.; Askerka, M.; Walters, G.; Gong, X. W.; Xing, J.; Wen, X. L.; Quintero-Bermudez, R.; Yuan, H. F.; Xing, G. C.; Wang, X. R.; Song, D. T.; Voznyy, O.; Zhang, M. T.; Hoogland, S.; Gao, W. B.; Xiong, Q. H.; Sargent, E. H., Spin control in reduced-dimensional chiral perovskites. *Nature Photonics* **2018,** *12* (9), 528-+.
7. Jana, M. K.; Song, R.; Liu, H.; Khanal, D. R.; Janke, S. M.; Zhao, R.; Liu, C.; Valy Vardeny, Z.; Blum, V.; Mitzi, D. B., Organic-to-inorganic structural chirality transfer in a 2D hybrid perovskite and impact on Rashba-Dresselhaus spin-orbit coupling. *Nat Commun* **2020,** *11* (1), 4699.
8. Lu, H. P.; Wang, J. Y.; Xiao, C. X.; Pan, X.; Chen, X. H.; Brunecky, R.; Berry, J. J.; Zhu, K.; Beard, M. C.; Vardeny, Z. V., Spin-dependent charge transport through 2D chiral hybrid lead-iodide perovskites. *Science Advances* **2019,** *5* (12).
9. Wang, J.; Lu, H.; Pan, X.; Xu, J.; Liu, H.; Liu, X.; Khanal, D. R.; Toney, M. F.; Beard, M. C.; Vardeny, Z. V., Spin-Dependent Photovoltaic and Photogalvanic Responses of Optoelectronic Devices Based on Chiral Two-Dimensional Hybrid Organic-Inorganic Perovskites. *ACS Nano* **2021,** *15* (1), 588-595.
10. Mitzi, D. B.; Chondroudis, K.; Kagan, C. R., Design, Structure, and Optical Properties of Organic-Inorganic Perovskites Containing an Oligothiophene Chromophore. *Inorg Chem* **1999,** *38* (26), 6246-6256.
11. Era, M.; Maeda, K.; Tsutsui, T., Enhanced phosphorescence from naphthalene-chromophore incorporated into lead bromide-based layered perovskite having organic-inorganic superlattice structure. *Chem Phys Lett* **1998,** *296* (3-4), 417-420.
12. Mitzi, D. B., Organic-inorganic perovskites containing trivalent metal halide layers: the templating influence of the organic cation layer. *Inorg Chem* **2000,** *39* (26), 6107-13.
13. Fujisawa, J.; Ishihara, T., Charge-transfer transitions between wires and spacers in an inorganic-organic quasi-one-dimensional crystal methylviologen lead iodide. *Physical Review B* **2004,** *70* (11), 2-5.
14. Fujisawa, J.; Tajima, N., Photoconductivity induced by wire-to-spacer charge-transfer transitions in an inorganic-organic hybrid quasi-one-dimensional crystal: Polaron excitation in the Urbach tail. *Physical Review B* **2005,** *72* (12), 1-6.
15. Maughan, A. E.; Kurzman, J. A.; Neilson, J. R., Hybrid inorganic-organic materials with an optoelectronically active aromatic cation: $(C_7H_7)_2SnI_6$ and $C_7H_7PbI_3$. *Inorg Chem* **2015,** *54* (1), 370-8.
16. Oswald, I. W. H.; Mozur, E. M.; Moseley, I. P.; Ahn, H.; Neilson, J. R., Hybrid Charge-Transfer Semiconductors: $(C_7H_7)SbI_4$, $(C_7H_7)BiI_4$, and Their Halide Congeners. *Inorg Chem* **2019,** *58* (9), 5818-5826.
17. Evans, H. A.; Lehner, A. J.; Labram, J. G.; Fabini, D. H.; Barreda, O.; Smock, S. R.; Wu, G.; Chabinyc, M. L.; Seshadri, R.; Wudl, F., (TTF)Pb2I5: A Radical Cation-Stabilized Hybrid Lead Iodide with Synergistic Optoelectronic Signatures. *Chemistry of Materials* **2016,** *28* (11), 3607-3611.
18. Dunlap-Shohl, W. A.; Barraza, E. T.; Barrette, A.; Dovletgeldi, S.; Findik, G.; Dirkes, D. J.; Liu, C.; Jana, M. K.; Blum, V.; You, W.; Gundogdu, K.; Stiff-Roberts, A. D.; Mitzi, D. B., Tunable internal quantum well alignment in rationally designed oligomer-based perovskite films deposited by resonant infrared matrix-assisted pulsed laser evaporation. *Mater Horiz* **2019,** *6* (8), 1707-1716.
19. Fujisawa, J.; Giorgi, G., Lead-iodide nanowire perovskite with methylviologen showing interfacial charge-transfer absorption: a DFT analysis. *Phys Chem Chem Phys* **2014,** *16* (33), 17955-9.

20. Sun, C.; Xu, G.; Jiang, X.-M.; Wang, G.-E.; Guo, P.-Y.; Wang, M.-S.; Guo, G.-C., Design Strategy for Improving Optical and Electrical Properties and Stability of Lead-Halide Semiconductors. *Journal of the American Chemical Society* **2018,** *140* (8), 2805-2811.
21. Zhao, L.; Lin, Y. L.; Kim, H.; Giebink, N. C.; Rand, B. P., Donor/Acceptor Charge-Transfer States at Two-Dimensional Metal Halide Perovskite and Organic Semiconductor Interfaces. *ACS Energy Letters* **2018,** *3* (11), 2708-2712.
22. Wang, G.-E.; Sun, C.; Wang, M.-S.; Guo, G.-C., Semiconducting crystalline inorganic–organic hybrid metal halide nanochains. *Nanoscale* **2020,** *12* (8), 4771-4789.
23. Febriansyah, B.; Koh, T. M.; John, R. A.; Ganguly, R.; Li, Y.; Bruno, A.; Mhaisalkar, S. G.; England, J., Inducing Panchromatic Absorption and Photoconductivity in Polycrystalline Molecular 1D Lead-Iodide Perovskites through π-Stacked Viologens. *Chemistry of Materials* **2018,** *30* (17), 5827-5830.
24. Liu, J. J.; Guan, Y. F.; Jiao, C.; Lin, M. J.; Huang, C. C.; Dai, W. X., A panchromatic hybrid crystal of iodoplumbate nanowires and J-aggregated naphthalene diimides with long-lived charge-separated states. *Dalton Trans* **2015,** *44* (13), 5957-60.
25. Liu, J. J.; Chen, Y.; Lin, M. J.; Huang, C. C.; Dai, W. X., Two-semiconductive-component hybrid coordination polymers with controllable photo-induced electron-transfer properties. *Dalton Trans* **2016,** *45* (15), 6339-42.
26. Maheshwari, S.; Savenije, T. J.; Renaud, N.; Grozema, F. C., Computational Design of Two-Dimensional Perovskites with Functional Organic Cations. *J Phys Chem C Nanomater Interfaces* **2018,** *122* (30), 17118-17122.
27. Li, X. M.; Yang, J.; Song, Z. Y.; Chen, R. P.; Ma, L. L.; Li, H. N.; Jia, J.; Meng, J.; Li, X.; Yi, M. D.; Sun, X., Naphthalene Diimide Ammonium Directed Single-Crystalline Perovskites with "Atypical" Ambipolar Charge Transport Signatures in Two-Dimensional Limit. *Acs Applied Energy Materials* **2018,** *1* (9), 4467-4472.
28. Tremblay, M. H.; Zeidell, A. M.; Rigin, S.; Tyznik, C.; Bacsa, J.; Zhang, Y.; Al Kurdi, K.; Jurchescu, O. D.; Timofeeva, T. V.; Barlow, S.; Marder, S. R., Structural Diversity in 2,2'-[Naphthalene-1,8:4,5-bis(dicarboximide)-N,N'-diyl]-bis(ethylammonium) Iodoplumbates. *Inorg Chem* **2020,** *59* (12), 8070-8080.
29. Bhosale, S. V.; Jani, C. H.; Langford, S. J., Chemistry of naphthalene diimides. *Chem Soc Rev* **2008,** *37* (2), 331-42.
30. Kobaisi, M. A.; Bhosale, S. V.; Latham, K.; Raynor, A. M.; Bhosale, S. V., Functional Naphthalene Diimides: Synthesis, Properties, and Applications. *Chem Rev* **2016,** *116* (19), 11685-11796.
31. Billing, D. G.; Lemmerer, A., Synthesis, characterization and phase transitions in the inorganic-organic layered perovskite-type hybrids [(CnH2n+1NH3)(2)PbI4], n=4, 5 and 6. *Acta Crystallographica Section B-structural Science* **2007,** *63*, 735-747.
32. Billing, D. G.; Lemmerer, A., Synthesis, characterization and phase transitions of the inorganic–organic layered perovskite-type hybrids $[(C_nH_{2n+1}NH_3)_2PbI_4]$ (n = 12, 14, 16 and 18). *New Journal of Chemistry* **2008,** *32* (10), 1736-1746.
33. Lemmerer, A.; Billing, D. G., Synthesis, characterization and phase transitions of the inorganic-organic layered perovskite-type hybrids $[(C_{(n)}H_{(2n+1)}NH_3)_2PbI_4]$, n = 7, 8, 9 and 10. *Dalton Trans* **2012,** *41* (4), 1146-57.
34. Gelvez-Rueda, M. C.; Fridriksson, M. B.; Dubey, R. K.; Jager, W. F.; van der Stam, W.; Grozema, F. C., Overcoming the exciton binding energy in two-dimensional perovskite nanoplatelets by attachment of conjugated organic chromophores. *Nat Commun* **2020,** *11* (1), 1901.
35. Lédée, F.; Trippé-Allard, G.; Diab, H.; Audebert, P.; Garrot, D.; Lauret, J.-S.; Deleporte, E., Fast growth of monocrystalline thin films of 2D layered hybrid perovskite. *CrystEngComm* **2017,** *19* (19), 2598-2602.

36. Tian, H.; Zhao, L.; Wang, X.; Yeh, Y. W.; Yao, N.; Rand, B. P.; Ren, T. L., Extremely Low Operating Current Resistive Memory Based on Exfoliated 2D Perovskite Single Crystals for Neuromorphic Computing. *ACS Nano* **2017,** *11* (12), 12247-12256.
37. Liu, Y.; Yang, Z.; Liu, S. F., Recent Progress in Single-Crystalline Perovskite Research Including Crystal Preparation, Property Evaluation, and Applications. *Adv Sci (Weinh)* **2018,** *5* (1), 1700471.
38. Shen, H.; Nan, R.; Jian, Z.; Li, X., Defect step controlled growth of perovskite $MAPbBr_3$ single crystal. *Journal of Materials Science* **2019,** *54* (17), 11596-11603.
39. Di, J.; Chang, J.; Liu, S., Recent progress of two-dimensional lead halide perovskite single crystals: Crystal growth, physical properties, and device applications. *EcoMat* **2020,** *2* (3).
40. Wu, Z.; Ji, C.; Wang, S.; Zhang, W.; Wang, Y.; Li, L.; Zhao, S.; Sun, Z.; Luo, J., (2-Methylpiperidine)PbI_3: an ABX_3-type organic–inorganic hybrid chain compound and its semiconducting nanowires with photoconductive properties. *Journal of Materials Chemistry C* **2017,** *5* (44), 11466-11471.
41. Wu, Z.; Li, L.; Ji, C.; Lin, G.; Wang, S.; Shen, Y.; Sun, Z.; Zhao, S.; Luo, J., Broad-Band-Emissive Organic-Inorganic Hybrid Semiconducting Nanowires Based on an ABX_3-Type Chain Compound. *Inorg Chem* **2017,** *56* (15), 8776-8781.
42. Pradeesh, K.; Agarwal, M.; Rao, K. K.; Prakash, G. V., Synthesis, crystal structure and optical properties of quasi-one-dimensional lead (II) iodide: $C_{14}H_{18}N_2Pb_2I_6$. *Solid State Sci* **2010,** *12* (1), 95-98.
43. Trigui, A.; Abid, H.; Mlayah, A.; Abid, Y., Optical properties and vibrational studies of a new self assembled organic–inorganic nanowire crystal $(C_6H_{13}N_3)_2Pb_3I_{10}$. *Synthetic Metals* **2012,** *162* (19-20), 1731-1736.
44. Zhai, Y.; Baniya, S.; Zhang, C.; Li, J.; Haney, P.; Sheng, C. X.; Ehrenfreund, E.; Vardeny, Z. V., Giant Rashba splitting in 2D organic-inorganic halide perovskites measured by transient spectroscopies. *Sci Adv* **2017,** *3* (7), e1700704.
45. Liu, W.; Shaikh, D. B.; Rao, P. S.; Bhosale, R. S.; Said, A. A.; Mak, A. M.; Wang, Z.; Zhao, M.; Gao, W.; Chen, B.; Lam, Y. M.; Fan, W.; Bhosale, S. V.; Bhosale, S. V.; Zhang, Q., Molecular Aggregation of Naphthalene Diimide(NDI) Derivatives in Electron Transport Layers of Inverted Perovskite Solar Cells and Their Influence on the Device Performance. *Chem Asian J* **2020,** *15* (1), 112-121.
46. Duan, H. B.; Zhao, H. R.; Ren, X. M.; Zhou, H.; Tian, Z. F.; Jin, W. Q., Inorganic-organic hybrid compounds based on face-sharing octahedral [PbI3]infinity chains: self-assemblies, crystal structures, and ferroelectric, photoluminescence properties. *Dalton Trans* **2011,** *40* (8), 1672-83.
47. Martinez, J. F.; La Porte, N. T.; Wasielewski, M. R., Electron Transfer from Photoexcited Naphthalene Diimide Radical Anion to Electrocatalytically Active $Re(bpy)(CO)_3Cl$ in a Molecular Triad. *The Journal of Physical Chemistry C* **2018,** *122* (5), 2608-2617.
48. Powell, D.; Campbell, E. V.; Flannery, L.; Ogle, J.; Soss, S. E.; Whittaker-Brooks, L., Steric hindrance dependence on the spin and morphology properties of highly oriented self-doped organic small molecule thin films. *Materials Advances* **2021,** *2* (1), 356-365.
49. Dawson, R. E.; Hennig, A.; Weimann, D. P.; Emery, D.; Ravikumar, V.; Montenegro, J.; Takeuchi, T.; Gabutti, S.; Mayor, M.; Mareda, J.; Schalley, C. A.; Matile, S., Experimental evidence for the functional relevance of anion-pi interactions. *Nat Chem* **2010,** *2* (7), 533-8.
50. Ferguson, A. J.; Reid, O. G.; Nanayakkara, S. U.; Ihly, R.; Blackburn, J. L., Efficiency of Charge-Transfer Doping in Organic Semiconductors Probed with Quantitative Microwave and Direct-Current Conductance. *J Phys Chem Lett* **2018,** *9* (23), 6864-6870.
51. Sulas-Kern, D. B.; Zhang, H. Y.; Li, Z. D.; Blackburn, J. L., Microsecond charge separation at heterojunctions between transition metal dichalcogenide monolayers and single-walled carbon nanotubes. *Materials Horizons* **2019,** *6* (10), 2103-2111.

52. Kang, H. S.; Sisto, T. J.; Peurifoy, S.; Arias, D. H.; Zhang, B. Y.; Nuckolls, C.; Blackburn, J. L., Long-Lived Charge Separation at Heterojunctions between Semiconducting Single-Walled Carbon Nanotubes and Perylene Diimide Electron Acceptors. *J Phys Chem C* **2018,** *122* (25), 14150-14161.
53. Savory, C. N.; Palgrave, R. G.; Bronstein, H.; Scanlon, D. O., Spatial Electron-hole Separation in a One Dimensional Hybrid Organic-Inorganic Lead Iodide. *Sci Rep* **2016,** *6*, 20626.
54. Colbeau-Justin, C.; Valenzuela, M. A., Time-resolved microwave conductivity (TRMC) a useful characterization tool for charge carrier transfer in photocatalysis: a short review. *Rev Mex Fis* **2013,** *59* (3), 191-200.
55. Reid, O. G.; Moore, D. T.; Li, Z.; Zhao, D. W.; Yan, Y. F.; Zhu, K.; Rumbles, G., Quantitative analysis of time-resolved microwave conductivity data. *J Phys D Appl Phys* **2017,** *50* (49).
56. Zhang, Q. L.; Yuan, X.; Feng, Y. F.; Larson, B. W.; Su, G. M.; Maung, Y. M.; Rujisamphan, N.; Li, Y. Y.; Yuan, J. Y.; Ma, W. L., Understanding the Interplay of Transport-Morphology-Performance in PBDB-T-Based Polymer Solar Cells. *Sol Rrl* **2020,** *4* (4), 1-8.
57. Savenije, T. J.; Ferguson, A. J.; Kopidakis, N.; Rumbles, G., Revealing the Dynamics of Charge Carriers in Polymer:Fullerene Blends Using Photoinduced Time-Resolved Microwave Conductivity. *J Phys Chem C* **2013,** *117* (46), 24085-24103.
58. Ihly, R.; Mistry, K. S.; Ferguson, A. J.; Clikeman, T. T.; Larson, B. W.; Reid, O.; Boltalina, O. V.; Strauss, S. H.; Rumbles, G.; Blackburn, J. L., Tuning the driving force for exciton dissociation in single-walled carbon nanotube heterojunctions. *Nat Chem* **2016,** *8* (6), 603-9.
59. Thouin, F.; Valverde-Chávez, D. A.; Quarti, C.; Cortecchia, D.; Bargigia, I.; Beljonne, D.; Petrozza, A.; Silva, C.; Srimath Kandada, A. R., Phonon coherences reveal the polaronic character of excitons in two-dimensional lead halide perovskites. *Nature Materials* **2019,** *18* (4), 349-356.
60. Gauthron, K.; Lauret, J. S.; Doyennette, L.; Lanty, G.; Al Choueiry, A.; Zhang, S. J.; Brehier, A.; Largeau, L.; Mauguin, O.; Bloch, J.; Deleporte, E., Optical spectroscopy of two-dimensional layered $(C_6H_5C_2H_4NH_3)_2PbI_4$ perovskite. *Opt Express* **2010,** *18* (6), 5912-9.
61. Sichert, J. A.; Tong, Y.; Mutz, N.; Vollmer, M.; Fischer, S.; Milowska, K. Z.; Garcia Cortadella, R.; Nickel, B.; Cardenas-Daw, C.; Stolarczyk, J. K.; Urban, A. S.; Feldmann, J., Quantum Size Effect in Organometal Halide Perovskite Nanoplatelets. *Nano Lett* **2015,** *15* (10), 6521-7.
62. Straus, D. B.; Kagan, C. R., Electrons, Excitons, and Phonons in Two-Dimensional Hybrid Perovskites: Connecting Structural, Optical, and Electronic Properties. *J Phys Chem Lett* **2018,** *9* (6), 1434-1447.
63. Blum, V.; Gehrke, R.; Hanke, F.; Havu, P.; Havu, V.; Ren, X.; Reuter, K.; Scheffler, M., Ab initio molecular simulations with numeric atom-centered orbitals. *Computer Physics Communications* **2009,** *180* (11), 2175-2196.
64. Levchenko, S. V.; Ren, X.; Wieferink, J.; Johanni, R.; Rinke, P.; Blum, V.; Scheffler, M., Hybrid functionals for large periodic systems in an all-electron, numeric atom-centered basis framework. *Computer Physics Communications* **2015,** *192*, 60-69.
65. Heyd, J.; Scuseria, G. E.; Ernzerhof, M., Hybrid functionals based on a screened Coulomb potential. *The Journal of chemical physics* **2003,** *118* (18), 8207-8215.
66. Krukau, A. V.; Vydrov, O. A.; Izmaylov, A. F.; Scuseria, G. E., Influence of the exchange screening parameter on the performance of screened hybrid functionals. *The Journal of chemical physics* **2006,** *125* (22), 224106.
67. Huhn, W. P.; Blum, V., One-hundred-three compound band-structure benchmark of post-self-consistent spin-orbit coupling treatments in density functional theory. *Physical Review Materials* **2017,** *1* (3), 033803.
68. Marques, M. A.; Vidal, J.; Oliveira, M. J.; Reining, L.; Botti, S., Density-based mixing parameter for hybrid functionals. *Phys Rev B* **2011,** *83* (3), 035119.

69. Kaduk, B.; Kowalczyk, T.; Van Voorhis, T., Constrained density functional theory. *Chemical reviews* **2012,** *112* (1), 321-370.
70. Cheng, C.-L.; Wu, Q.; Van Voorhis, T., Rydberg energies using excited state density functional theory. *The Journal of chemical physics* **2008,** *129* (12), 124112.
71. Gavnholt, J.; Olsen, T.; Engelund, M.; Schiøtz, J., Δ self-consistent field method to obtain potential energy surfaces of excited molecules on surfaces. *Phys Rev B* **2008,** *78* (7), 075441.
72. Padgaonkar, S.; Amsterdam, S. H.; Bergeron, H.; Su, K.; Marks, T. J.; Hersam, M. C.; Weiss, E. A., Molecular-Orientation-Dependent Interfacial Charge Transfer in Phthalocyanine/MoS_2 Mixed-Dimensional Heterojunctions. *J Phys Chem C* **2019,** *123* (21), 13337-13343.
73. Ball, J. M.; Stranks, S. D.; Hoerantner, M. T.; Huettner, S.; Zhang, W.; Crossland, E. J. W.; Ramirez, I.; Riede, M.; Johnston, M. B.; Friend, R. H.; Snaith, H. J., Optical properties and limiting photocurrent of thin-film perovskite solar cells. *Energy & Environmental Science* **2015,** *8* (2), 602-609.
74. Sheldrick, G. M., SHELXT - integrated space-group and crystal-structure determination. *Acta Crystallogr A Found Adv* **2015,** *71* (Pt 1), 3-8.
75. Dolomanov, O. V.; Bourhis, L. J.; Gildea, R. J.; Howard, J. A. K.; Puschmann, H., OLEX2: a complete structure solution, refinement and analysis program. *J Appl Crystallogr* **2009,** *42* (2), 339-341.